Article

# Manipulating the Spin State of Co Sites in Metal−Organic Frameworks for Boosting CO$_2$ Photoreduction

Kang Sun,[#] Yan Huang,[#] Qingyu Wang, Wendi Zhao, Xusheng Zheng, Jun Jiang,* and Hai-Long Jiang*

Read Online

ACCESS | Metrics & More | Article Recommendations | Supporting Information

**ABSTRACT:** Photocatalytic CO$_2$ reduction holds great potential for alleviating global energy and environmental issues, where the electronic structure of the catalytic center plays a crucial role. However, the spin state, a key descriptor of electronic properties, is largely overlooked. Herein, we present a simple strategy to regulate the spin states of catalytic Co centers by changing their coordination environment by exchanging the Co species into a stable Zn-based metal−organic framework (MOF) to afford **Co-OAc**, **Co-Br**, and **Co-CN** for CO$_2$ photoreduction. Experimental and DFT calculation results suggest that the distinct spin states of the Co sites give rise to different charge separation abilities and energy barriers for CO$_2$ adsorption/activation in photocatalysis. Consequently, the optimized **Co-OAc** with the highest spin-state Co sites presents an excellent photocatalytic CO$_2$ activity of 2325.7 $\mu$mol·g$^{-1}$·h$^{-1}$ and selectivity of 99.1% to CO, which are among the best in all reported MOF photocatalysts, in the absence of a noble metal and additional photosensitizer. This work underlines the potential of MOFs as an ideal platform for spin-state manipulation toward improved photocatalysis.
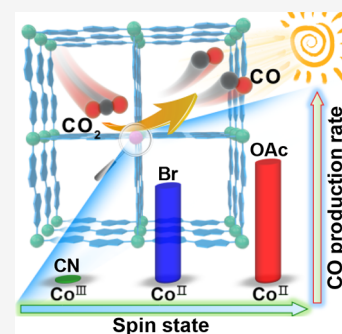
## INTRODUCTION

The energy crisis and greenhouse effect seriously threaten the sustainable development of society. The utilization of abundant solar energy to convert CO$_2$ into chemical fuels is recognized as one of the promising solutions.[1] However, CO$_2$ photoreduction usually suffers from low efficiency since CO$_2$ is a stable symmetric molecule with high C=O bond energy as well as ease of charge recombination in photocatalysts.[2−4] The suppression of photogenerated charge recombination and promotion of CO$_2$ adsorption and activation are crucial for efficient photocatalytic CO$_2$ reduction. So far, many strategies have been developed to enhance charge separation and facilitate CO$_2$ adsorption and activation for CO$_2$ photoreduction.[5−10]

Electronic structures determine the properties of materials, in which spin is an important inherent characteristic of electrons and can reflect the electronic structures of catalysts, dominating the chemical behavior of catalysts.[11,12] Recently, theoretical predictions and experiments have demonstrated that spin regulation enables improved catalytic performance.[13−17] However, there have been very limited examples on spin regulation in photocatalysis, especially for photocatalytic CO$_2$ reduction,[18−20] which is probably due to the grand challenge of regulating spin states in common photocatalysts. Currently, spin-state regulation in heterogeneous photocatalysts is mainly limited to the creation of structural vacancies and elemental doping.[13−16,19] Unfortunately, vacancies and dopants are not definitely catalytically active for CO$_2$ reduction, and sometimes, vacancies are even recombination centers of electrons and holes.[3] Meanwhile, vacancies and dopants in catalysts are not homogeneously distributed, and

accordingly, only the local spin state is changed. Therefore, the creation of vacancies and elemental doping in photocatalysts remain a challenge not only in precise fabrication but also in the establishment of the relationship between spin-state regulation and photocatalysis.

As a class of emerging photocatalysts, metal−organic frameworks (MOFs), constructed by metal nodes and organic linkers, featuring atomically precise and highly tailorable structures,[21−24] are excellent candidates for understanding the relationship between the structure and performance.[25−31] The d-transition metal nodes in MOFs are commonly recognized as excellent active sites for CO$_2$ photoreduction,[32−39] whose performance should be strongly sensitive to the metal spin state. Significantly, the metal nodes, dominating the photocatalysis, are allowed to be decorated and/or substituted without disturbing the MOF skeleton and photoresponse.[40−44] Therefore, MOFs might be an ideal platform to regulate the spin state for enhanced CO$_2$ photoreduction.
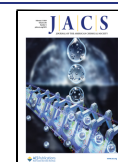
Herein, Zn(II) sites are partially substituted with Co(II)/Co(III) in a stable Zn-based MOF, CFA-1,[45] by a facile postsynthetic exchange strategy. By altering the type of Co precursor, three different counterparts bearing Co centers

coordinated with −CH₃COO, −Br, and −CN have been synthesized to afford **Co-OAc**, **Co-Br**, and **Co-CN**, respectively (Scheme 1). Both experimental and DFT calculations

**Scheme 1. Synthesis of Co-OAc, Co-Br, and Co-CN Featuring Different Spin States of Co^II and Co^III Species via a Postsynthetic Exchange Strategy**
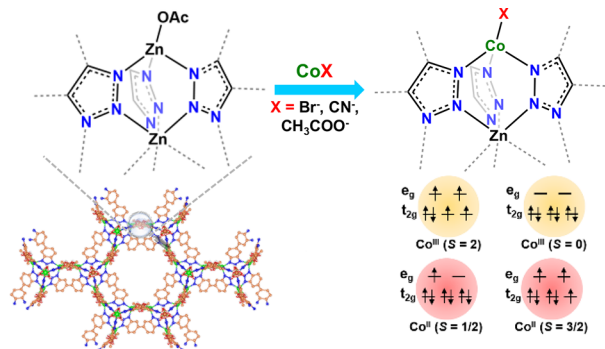
suggest that the modulation of the coordination microenvironment of the Co sites gives rise to its spin-state regulation with or without changing the Co oxidation state, leading to differentiated charge separation efficiency as well as $CO_2$ adsorption and activation. As a result, **Co-OAc** with the highest spin state possesses superior charge separation and optimized energy barriers of $CO_2$ adsorption and activation, thereby presenting an excellent photocatalytic $CO_2$ reduction rate of 2325.7 $\mu$mol·g$^{-1}$·h$^{-1}$ with 99.1% selectivity to CO, which is among the best in all MOF photocatalysts, in the absence of a noble metal and additional photosensitizer.

## ◼ RESULTS AND DISCUSSION

A representative MOF, namely, CFA-1, was synthesized based on a facile solvothermal method with the linker 1*H*,1'*H*-5,5'-bibenzo[*d*][1,2,3]triazole and zinc acetate dihydrate at 120 °C. By postsynthetic exchanging the 5-fold-coordinated Zn(II) sites in CFA-1 with different Co precursors, e.g., Co(OAc)₂· 4H₂O, CoBr₂·xH₂O, and K₃[Co(CN)₆], under solvothermal conditions,[45] the corresponding products, **Co-OAc**, **Co-Br**, and **Co-CN** were respectively obtained, where the Co contents are all ∼1.0 wt % based on the inductively coupled plasma atomic emission spectroscopy (ICP-AES) results. The powder X-ray diffraction (XRD) patterns manifest the maintained crystallinity of all of the Co counterparts after postsynthetic exchange (Figure S1). To identify the coordination environment of the Co sites, X-ray absorption fine structure (XAFS) spectroscopy has been conducted. The Fourier transform-extended X-ray absorption fine structure (FT-EXAFS) spectrum of **Co-OAc** presents a dominant peak at ∼1.58 Å that can be ascribed to the Co−O bond or Co−N bond, while the Co−Co bond is not observable (Figure S2), indicating that the Co sites are dispersed atomically in the MOF skeleton. Furthermore, the curve fitting for the EXAFS data indicates that each Co site is coordinated with three linkers and one acetate (Figure 1a and Table S1). Similarly, the Co sites in **Co-Br** and **Co-CN** are coordinated with one Br⁻ and two CN⁻, respectively, as verified by the XAFS (Figures S3 and S4 and Table S1). The scanning electron microscopy (SEM) images and gas sorption isotherms indicate that there is no obvious difference in the morphologies, porous features, and $CO_2$ adsorption capacities of all these counterparts (Figures S5−
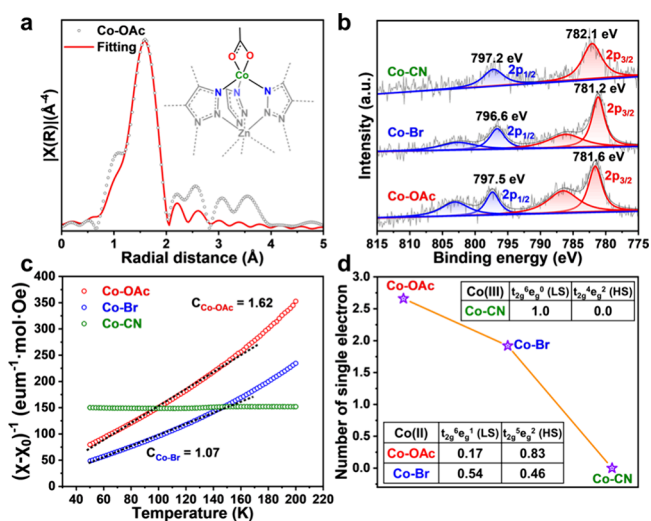


**Figure 1.** (a) Co K-edge EXAFS spectrum fitting for **Co-OAc** and (inset) optimized coordination structure of the involved Co site. (b) XPS spectra of Co 2p for **Co-OAc**, **Co-Br**, and **Co-CN**. (c) Fitted susceptibility vs temperature based on Curie−Weiss law for **Co-OAc**, **Co-Br**, and **Co-CN** (*C* is the Curie constant obtained from the slope of the curve). (d) Number of single electrons and the corresponding fraction of HS and LS states for **Co-OAc**, **Co-Br**, and **Co-CN**.

S8). Moreover, the energy band structures have been further evaluated by Tauc and Mott−Schottky plots (Figures S9−S11). All Co-based MOF counterparts exhibit similar light absorption, optical band gaps, and HOMO (highest occupied molecular orbital) and LUMO (lowest unoccupied molecular orbital) levels, suggesting their similar redox capabilities in photocatalysis. All of the above results demonstrate that the coordination microenvironment of Co sites would be the only variable in **Co-OAc**, **Co-Br**, and **Co-CN**.

In view of the similar physicochemical properties of all of these Co counterparts, the spin features of the involved Co species have been investigated. It is assumed that the different coordination microenvironments of Co sites would strongly affect their electronic structures, which would then give rise to perturbation of their spin states, regardless of the Co oxidation state. For example, the two electron configurations, i.e., $t_{2g}^6 e_g^1$ and $t_{2g}^5 e_g^2$, of Co^II are associated with its low spin (LS) and high spin (HS) states, respectively, while the LS and HS states are $t_{2g}^6 e_g^0$ and $t_{2g}^4 e_g^2$, respectively, for Co^III (Scheme 1). X-ray photoelectron spectroscopy (XPS) was performed to reveal the electronic structure and oxidation states of Co sites in the MOFs. The two apparent satellite peaks indicate the +2 oxidation state of the Co species in **Co-OAc** and **Co-Br**, whereas there is no satellite peak in **Co-CN**, reflecting its +3 oxidation state (Figure 1b and Figure S12).[18] Given that the energy difference between Co $2p_{1/2}$ and Co $2p_{3/2}$, referred to as spin−orbit splitting ($\Delta E$), would increase as the number of single electrons in the Co center increased,[46,47] the obtained $\Delta E$ in the order of $\Delta E_{\text{Co-OAc}}$ (15.9 eV) > $\Delta E_{\text{Co-Br}}$ (15.4 eV) > $\Delta E_{\text{Co-CN}}$ (15.1 eV) suggests that the Co species in **Co-OAc** might present a higher spin state than those in **Co-Br** and **Co-CN** (Figure 1b). These results preliminarily indicate that regulation of the Co coordination environment can change its electronic structure and spin state.

To further elucidate the influence of coordination atoms on the spin state of the Co site, theoretical calculations have been performed. Density functional theory (DFT) calculation

results show that the energy of **Co-OAc** with low-spin $Co^{II}$ sites ($S = 1/2$) is 0.56 eV higher than that with high-spin $Co^{II}$ sites ($S = 3/2$) in **Co-OAc**, reflecting that the $Co^{II}$ sites in **Co-OAc** tend to be in a high spin state (Table S2). In contrast, **Co-Br** has comparable energies for both the low-spin and high-spin $Co^{II}$, which suggests that both spin states are possible. In addition, the much lower energy observed for **Co-CN** with $Co^{III}$ at a low spin state ($S = 0$) than those at higher spin states ($S = 1, 2$) implies the absence of single electrons for $Co^{III}$ sites in **Co-CN**. Overall, the DFT results indicate that the spin state of Co species follows the order **Co-OAc** > **Co-Br** > **Co-CN**, which is consistent with the above XPS results. To verify the DFT results, temperature-dependent magnetization measurements have been carried out, which is a technique that can be used to determine the exact single electron number of Co sites.[48,49] The magnetic susceptibility of CFA-1 does not vary with temperature, manifesting its diamagnetic feature (Figure S13a). As expected, **Co-CN** also presents a diamagnetic behavior (Figure S13b), confirming its electron configuration of $t_{2g}^{6}e_{g}^{0}$ without a single 3d electron ($S = 0$), in agreement with the DFT results. Unlike CFA-1 and **Co-CN**, the magnetic susceptibilities support the paramagnetic feature of **Co-Ac** and **Co-Br**. By fitting the magnetic susceptibilities based on the modified Curie–Weiss law, the effective magnetic moment ($\mu_{eff}$) of **Co-Ac** and **Co-Br** can be calculated to be 3.60 $\mu_B$ and 2.93 $\mu_B$, respectively (Figure 1c,d and Figures S14 and S15).[48] Based on the relationship between the $\mu_{eff}$ and spin state, the spin states of **Co-Ac** and **Co-Br** can be calculated as 0.17 LS + 0.83 HS and 0.54 LS + 0.46 HS, respectively, corresponding to 2.66 and 1.92 of the single 3d electron numbers,[49] which well approve the DFT calculation results.

Encouraged by the above results, visible-light-driven photocatalytic $CO_2$ reduction has been proceeded in the absence of an additional photosensitizer and noble metal cocatalyst. The photocatalytic experiments indicate that **Co-OAc** exhibits $H_2$, CO, and $CH_4$ production rates of 18.3, 2325.7, and 1.8 $\mu mol \cdot g^{-1} \cdot h^{-1}$, respectively, corresponding to a turnover frequency (TOF) for CO of 27.0 $h^{-1}$ and a high CO selectivity of 99.1% (Figure 2a, Figure S16, and Table S3). No liquid products can

be found based on ion chromatography and NMR results (Figures S17 and S18). The activity and selectivity of **Co-OAc** are among the best compared to reported MOF photocatalysts and even surpass most heterogeneous photocatalysts in the absence of an additional photosensitizer and noble metal (Tables S4 and S5). No carbon products can be found with $N_2$ instead of $CO_2$ as the feeding gas or in the absence of light irradiation (Table S3), which suggests that $CO_2$ and light irradiation are indispensable for the $CO_2$ photoreduction. To clarify the origin of CO, the $^{13}CO_2$ isotopic labeling experiment has been completed with gas chromatography–mass spectrometry (GC-MS). The total ion chromatography (TIC) peak at 6.3 min corresponds to the CO product, whose MS mainly consists of three signals. The signal at $m/z = 29$ is assignable to $^{13}CO$, and the $^{13}C$ at $m/z = 13$ and O at $m/z = 16$ are ascribed to the fragments of $^{13}CO$, confirming that CO originates from the $CO_2$ conversion (Figure 2b). The recycling experiment for **Co-OAc** suggests that no noticeable decrease in the CO production activity can be observed, demonstrating its high stability in photocatalysis (Figure 2c). The leaching of Co and degradation of linkers are negligible in the supernatant after the reaction (Figure S18). Furthermore, powder XRD patterns support the maintained structural integrity and crystallinity (Figure S19). In addition, the photocatalytic performances of **Co-Br** and **Co-CN** have been investigated to uncover the impact of the Co spin state on the photocatalytic $CO_2$ reduction. Despite the fact that both **Co-Br** and **Co-CN** exhibit a high CO selectivity of >97%, compared with **Co-OAc**, the CO production rate over **Co-Br** with low spin-state $Co^{II}$ sites shows a slight decrease (1864.4 $\mu mol \cdot g^{-1} \cdot h^{-1}$) with a TOF of 11.2 $h^{-1}$, and the CO activity is only 57.3 $\mu mol \cdot g^{-1} \cdot h^{-1}$ with a TOF of 0.4 $h^{-1}$ over **Co-CN**, which is less than one fortieth of **Co-OAc** (Figure 2a and Table S3). As a control, no CO can be observed for CFA-1. Furthermore, the CO activity and selectivity of physically mixed CFA-1 and the corresponding cobalt salts, including $Co(OAc)_2 \cdot 4H_2O$, $CoBr_2 \cdot xH_2O$ and $K_3[Co(CN)_6]$, are significantly decreased (Table S3). These results indicate that the active sites responsible for $CO_2$ reduction are the Co sites with different coordination environments rather than the Zn sites or the homogeneous cobalt salts, confirming the influence of different spin states of Co species on the $CO_2$ reduction. To further correlate the spin state and photocatalytic activity, the relationship between the CO activity and the number of single electrons is presented (Figure 2d), which indicates the boosting of the CO production rate along with an increased number of single electrons, unambiguously unveiling the remarkable influence of Co spin states on the $CO_2$ photoreduction activity. In addition, the photocatalytic performance over the three MOF counterparts under both full spectrum irradiation and simulated sunlight has been evaluated (Table S3). The excellent performances indicate the good light-harvesting capability of these Co-based MOFs.

To unveil the charge transfer mechanism in photocatalysis, *in situ* soft X-ray absorption spectroscopy (sXAS) and *in situ* electron paramagnetic resonance (EPR) have been performed over **Co-OAc** as a representative. The peaks at 778.4 and 793.7 eV correspond to the $L_3$ and $L_2$ edges, respectively (Figure 3a), which arise from the electron transition from p-orbitals to d-orbitals.[50] Notably, the signals under light irradiation are apparently suppressed, suggesting that the Co sites accept electrons.[50] Furthermore, *in situ* EPR shows a $Co^{2+}$ signal under dark conditions (Figure S20).[51] Upon exposure to light,
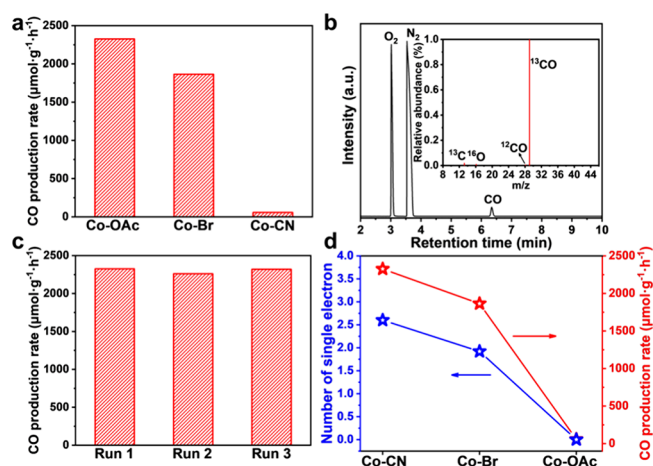


**Figure 2.** (a) Photocatalytic CO production rate over **Co-OAc**, **Co-Br**, and **Co-CN**. (b) Total ion chromatography signals and (inset) mass spectra for the $^{13}CO$ product in photocatalytic $^{13}CO_2$ reduction over **Co-OAc**. (c) Recycling performance of **Co-OAc**. (d) Relationship between the CO production rate and the single electron numbers of the Co species in **Co-OAc**, **Co-Br**, and **Co-CN**.
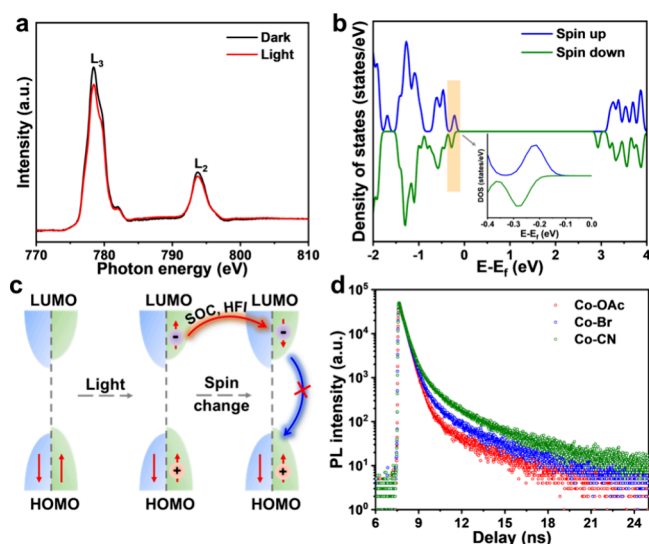
**Figure 3.** (a) *In situ* Co L-edge sXAS spectra for **Co-OAc** in the dark and under light irradiation. (b) Density of states of **Co-OAc** (the inset is an enlarged DOS diagram around HOMO). (c) Mechanism of spin polarization for improved charge separation. (d) Time-resolved PL spectra of **Co-OAc**, **Co-Br**, and **Co-CN**.

a reduced signal can be observed as the $Co^{2+}$ accepting electrons is converted into EPR-silent $Co^+$. When $CO_2$ is introduced, the signal is partially restored, implying the electron migration from Co sites to $CO_2$.[52] Therefore, we can conclude that Co sites are reduced after accepting photogenerated electrons in the photocatalytic process; subsequently, the electrons are transferred to $CO_2$, thereby achieving the photocatalytic reaction.

There are three key factors that govern a photocatalytic reaction efficiency, namely, light absorption, charge separation, and surface reactions. In view of the similar light absorption of the three Co-based MOFs, the charge separation process and $CO_2$ adsorption and activation have been examined to elucidate how the spin state of Co sites affects the $CO_2$ photoreduction activity. The different spin states usually give rise to discriminative spin polarization that affects charge separation.[16,19] Therefore, the density of states (DOS) plots have been calculated to show the spin-polarized electron distributions of these photocatalysts. As expected, no spin-polarized behavior is observed for CFA-1 and **Co-CN** due to their diamagnetism (Figures S21 and S22). In contrast, obvious spin-polarized electrons can be observed around HOMO (corresponding to the valence band maximum, VBM) for **Co-OAc** and **Co-Br** (Figures 3b and Figure S23), in which **Co-OAc** displays a higher spin polarization with more spin-up electrons, disclosing its superior charge separation.

To better understand how spin polarization leads to enhanced charge separation, a related mechanism is illuminated (Figure 3c). Under light irradiation, the spin-up electrons are excited to the LUMO (corresponds to the conduction band minimum, CBM), and the corresponding holes with the spin-up direction are left in HOMO. The photoexcited spin-up electrons will change their spin direction to spin down due to the spin−orbital coupling (SOC), hyperfine interaction (HFI), etc., while the spin-up holes remaining in the HOMO keep their spin direction.[16,19] In this case, the charge recombination will be suppressed due to the spin mismatch of photoexcited electrons and holes,[16] which

illustrates that a high degree of spin polarization will bring about enhanced charge separation.

Photo/electrochemical characterizations have been further performed to examine the boosted charge separation by spin polarization. The positive slopes of Mott−Schottky plots over the three Co-based MOFs indicate their *n*-type semiconducting nature, with electrons as the majority carriers. The carrier density can be estimated by the slope of the curve, where a high slope means a low carrier density.[53] It is apparent that the slope of **Co-OAc** is smaller than those of **Co-CN** and **Co-Br**, manifesting more photogenerated carriers in **Co-OAc** (Figure S24), which supports the idea that **Co-OAc** is able to produce more photogenerated carriers to participate in $CO_2$ photoreduction. The linear sweep voltammetry (LSV) profiles display the lowest onset overpotential and the fastest current growth at a higher voltage of **Co-OAc** (Figure S25), suggesting the superior charge transfer behavior of **Co-OAc** compared to **Co-Br** and **Co-CN**. The LSV results are further supported by the smallest radius of **Co-OAc** in the electrochemical impedance spectroscopy (EIS) plots and the strongest photocurrent response (Figures S26 and S27). To verify the electrochemical results, the steady-state and time-resolved photoluminescence (PL) spectra have been collected. The steady-state PL spectra of all the Co-based MOFs give similar emission signals centered at ~450 nm under excitation at 360 nm, whereas the fluorescence intensities of **Co-Br** and **Co-OAc** are significantly quenched and follow the intensity sequence of **Co-Br** > **Co-OAc** compared with the apparent emission of **Co-CN** (Figure S28). The fluorescence emission usually originates from the recombination process of excited electrons and holes; therefore, the sequence of the fluorescence intensity reversely matches the charge separation efficiency. In addition, **Co-OAc** presents a faster fluorescence decay than **Co-Br** and **Co-CN**, well demonstrating that more electrons in **Co-OAc** are separated and available for driving the photocatalytic $CO_2$ reactions (Figure 3d, Figures S29−S31).

The above results ambiguously demonstrate that spin-state regulation in Co-based MOFs can significantly promote charge separation for improving photocatalytic $CO_2$ reduction. Apart from the charge separation, the spin-state change also correlates with the perturbation of the Co electronic structure, which will affect the interaction between $CO_2$ and catalytic sites, leading to a different $CO_2$ adsorption and activation. Initially, *in situ* diffuse reflectance infrared Fourier transform spectroscopy (DRIFTS) has been adopted to identify the key intermediates in photocatalytic $CO_2$ reduction over **Co-OAc**. It is evident that some peaks of key intermediates are gradually enhanced with prolonged exposure to light irradiation (Figure 4a). The peaks at 1248 and 1325 $cm^{-1}$ can be assigned to $*CO_2^-$ and $CO_3^{2-}$, respectively, originating from the $CO_2$ activation process on the MOF surface.[54] More importantly, the *COOH intermediate is observed at 1549 $cm^{-1}$, which is commonly identified as key active species for reducing $CO_2$ to CO.[10,35] In addition, the signal of CO chemisorption at approximately 2022 $cm^{-1}$ supports CO as the main product during $CO_2$ reduction.[55] In terms of the DRIFTS results, a possible mechanism for the conversion of $CO_2$ to CO can be proposed: (1) $CO_2 \rightarrow CO_2^*$; (2) $CO_2^* + e^- + H^+ \rightarrow *COOH$; (3) $*COOH + e^- + H^+ \rightarrow *CO + H_2O$; and (4) $*CO \rightarrow CO$.

Following the reaction mechanism, theoretical calculations are further conducted to uncover the role of spin state regulation in $CO_2$ photoreduction. The adsorption of $CO_2$ on
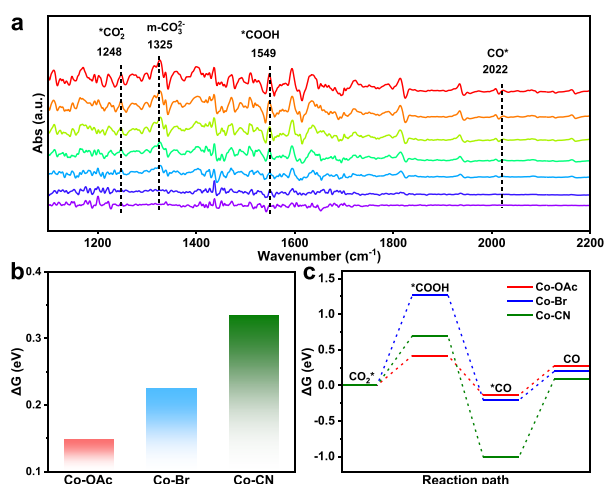
**Figure 4.** (a) *In situ* DRIFTS spectra for detecting the reaction intermediates in $CO_2$ photoreduction over **Co-OAc** under visible light irradiation. (b) Energy barrier of $CO_2$ adsorption on the surfaces of the three Co-based MOFs. (c) Energy variations of $CO_2$ photo-reduction along the reaction path of the three Co-based MOFs.

catalytic Co sites is the first step. DFT calculation results indicate that the adsorption energy barrier of $CO_2$ on the surface of the three catalysts follows a trend of **Co-CN** > **Co-Br** > **Co-OAc** (Figure 4b), revealing that the high-spin Co sites with more single electrons favor the stronger interaction between $CO_2$ and catalytic Co sites. Furthermore, the activation processes from adsorbed $CO_2$ (*$CO_2$) to oxidized CO have been examined. The Gibbs free energy ($\Delta G$) variation along the reaction paths via two hydrogenation steps is illustrated (Figure 4c). The formation of *COOH intermediates with the highest energy barrier is the rate-determining step (RDS) for **Co-OAc** and **Co-Br**, where the much lower energy barrier of **Co-OAc** supports the superior activity of **Co-OAc** to **Co-Br**. By contrast, the desorption of *CO is the RDS for **Co-CN**, the energy barrier of which is much higher than those of **Co-OAc** and **Co-Br**, indicating that the generated CO might not easily escape from the **Co-CN** surface in time, thus impeding the reaction. Consequently, the maximum resistances of $CO_2$ adsorption and CO desorption accompanied by the most suppressed charge separation in **Co-CN** result in its lowest photocatalytic activity.

## CONCLUSIONS

In summary, the substitution of 5-fold-coordinated Zn(II) in CFA-Zn by Co species with different Co precursors leads to the fabrication of three Co-based MOFs, namely, **Co-OAc**, **Co-Br**, and **Co-CN**, which feature very similar structures, light absorption, and energy band levels yet different coordination microenvironments of Co sites. Both experimental and calculation results demonstrate the regulated spin state of Co sites, i.e., **Co-OAc** > **Co-Br** > **Co-CN**, creating ideal models to investigate how the spin states of catalytic Co sites affect photocatalysis. In photocatalytic $CO_2$ reduction, **Co-OAc** with the highest spin-state Co sites exhibits an excellent photocatalytic CO production rate up to 2325.7 $\mu$mol·g$^{-1}$·h$^{-1}$ without a noble metal or additional photosensitizer, which is superior to the other counterparts. Results suggest that the spin-state regulation of catalytic Co centers can not only improve photoinduced charge separation but also optimize $CO_2$ adsorption and activation, thereby boosting the $CO_2$

photoreduction. This work achieves spin-state regulation in photocatalysts by altering the coordination microenvironments of catalytic metal sites and highlights the significant roles of metal spin states in photocatalysis.

## MATERIALS AND METHODS

**Materials and Equipment.** All chemicals were purchased from commercial sources and used without any further purification unless otherwise stated.

All powder X-ray diffraction (XRD) patterns were collected on a Rigaku MiniFlex 600 equipped with graphite-monochromated Cu K$\alpha$ radiation ($\lambda$ = 1.54178 Å). $N_2$ and $CO_2$ sorption isotherms were acquired by using automatic volumetric adsorption equipment (Micromeritics ASAP 2020). Scanning electron microscopy (SEM) images were taken on a Zeiss Supra 40 scanning electron microscope at an acceleration voltage of 5 kV. X-ray photoelectron spectroscopy (XPS) measurements were performed by using a Kratos Axis supra+ spectrometer equipped with monochromatized Al K$\alpha$ ($h\nu$ = 1486.6 eV) as the excitation source. The EPR measurements were conducted with a Bruker Nano X-band spectrometer at 100 K. The contents Co in the photocatalysts were quantified by an inductively coupled plasma atomic emission spectrometer (ICP-AES, Thermo Scientific iCAP 7400). The UV−vis diffuse reflectance spectra of the samples were collected by using a Shimadzu UV-2700. The steady-state photoluminescence emission spectra were obtained over a Fluorescence Spectrophotometer F-4600 made by HITACHI. The temperature-dependent magnetization measurements were carried out by a magnetic measuring system (Quantum Design MPMS3) with a magnetic field strength of 1 kOe. The photocatalytic gaseous products were analyzed by gas chromatography (GC, Agilent 8860) equipped with a thermal conductivity detector (TCD) and a flame ionization detector (FID) using Ar as the carrier gas. The photocatalytic liquid products were analyzed by an ion chromatograph (Thermo Scientific Dionex Aquion) and $^1$H nuclear magnetic resonance (NMR, Bruker AVANCE AV III 400). The $^{13}$C isotope-labeled products were analyzed by gas chromatography−mass spectrometry (GC-MS, Agilent Technologies 7890B GC-Agilent Technologies 5977B MSD Mass Spectrometer).

**Synthesis of 1$H$,1′$H$-5,5′-Bibenzo[$d$][1,2,3]triazole.** The ligand 1$H$,1′$H$-5,5′-bibenzo[$d$][1,2,3]triazole ($H_2$bibta) was synthesized following the reported method with some modifications.[45] Typically, 1 g of 3,3′,4,4′-tetraaminobiphenyl was dissolved in 10.0 mL of $CH_3$COOH, and then, 1.0 mL of $H_2$O was added. Then, 1.0 mL of $NaNO_2$ aqueous solution (0.70 g/mL) was added dropwise into the above solution under stirring. The reaction was stirred for 2 h in an ice−water bath. The product was collected by filtration and washed with $H_2$O and methanol three times.

**Synthesis of CFA-1.** CFA-1 was synthesized following the reported method with some modifications.[56] Typically, 1.48 g of $Zn(CH_3COO)_2$·4$H_2$O and 0.40 g of 3,3′-diaminobenzidine were dispersed into 200.0 mL of $N$,$N$-dimethylformamide (DMF) followed by adding 8.0 mL of $CH_3$COOH. The mixture was heated to 120 °C for 48 h. After cooling down to room temperature, the sample was filtered and washed with DMF, methanol, and acetone. Finally, the product was activated under vacuum for 12 h at 150 °C.

**Synthesis of Co-OAc.** Typically, 50.0 mg of CFA-1 was added into 9.0 mL of DMF in a 20 mL glass vial. Then, a 1.0 mL solution (2.5 mg/mL) of $Co(CH_3COO)_2$·4$H_2$O in DMF was added. The mixture was reacted at 60 °C for 24 h without stirring. The product was collected by centrifugation and washed three times with DMF and acetone. Finally, the product was activated under vacuum for 12 h at 150 °C. The Co loading amount is about 0.95 wt % based on ICP-AES results.

**Synthesis of Co-Br.** Typically, 50.0 mg of CFA-1 was added into 8.7 mL of DMF in a 20 mL glass vial. Then, a 1.3 mL solution (2.2 mg/mL) of $CoBr_2$·$x$H$_2$O in DMF was added. The mixture was reacted at 60 °C for 24 h without stirring. The product was collected by centrifugation and washed three times with DMF and acetone.

Finally, the product was activated under vacuum for 12 h at 150 °C. The Co loading amount is about 0.98 wt % based on ICP-AES results.

**Synthesis of Co-CN.** Typically, 50.0 mg of CFA-1 was added into 7.2 mL of DMF in a 20 mL glass vial. Then, 2.8 mL of $K_3[Co(CN)_6]$ aqueous solution (3.3 mg/mL) was added. The mixture was reacted at 60 °C for 24 h without stirring. The product was collected by centrifugation and washed three times with $H_2O$ and acetone. Finally, the product was activated under vacuum for 12 h at 150 °C. The Co loading amount is about 0.96 wt % based on ICP-AES results.

**Synthesis of 1,3-Dimethyl-2-phenyl-2,3-dihydro-1*H*-benzo-[*d*]imidazole (BIH).** BIH was synthesized following the reported method with some modifications.[57] Typically, 0.3 g of NaOH was added into 9.5 mL of methanol, and then, 1.5 g of 2-phenyl-benzimidazole and 4.0 g of methyl iodide were dissolved in the methanol solution. The solution was sealed in a pressure tube and reacted for 12 h at 110 °C. Then, the obtained crude product was filtered and washed with EtOH:$H_2O$ (5:1 v/v). The faint yellow precipitates were recrystallized from ethanol. The resulting product (3.0 g) was further dissolved in 80.0 mL of methanol, and 1.2 g of $NaBH_4$ was slowly added into the solution under a $N_2$ atmosphere. Then, the mixture was stirred for 1 h under a $N_2$ atmosphere in an ice−water bath. The products were collected by vacuum rotary evaporation, and the precipitates were recrystallized from EtOH:$H_2O$ (2:1 v/v) to obtain BIH crystals.

**Photoelectrochemical Measurements.** Mott−Schottky plot measurements and electrochemical impedance spectroscopy (EIS) were performed on a Zahner Zennium electrochemical workstation. Typically, 2 mg of photocatalyst was dispersed into 2 mL of ethanol and 10 $\mu$L of Nafion mixed solution. After ultrasonic uniformity, 30 $\mu$L of solution was dropped onto glassy carbon, used as a working electrode. The measurements were carried out using a three-electrode system with a Pt plate as a counter electrode and Ag/AgCl as a reference electrode. A 0.1 M $Na_2SO_4$ solution was used as the electrolyte.

The frequencies of the Mott−Schottky plot measurements were 500, 1000, and 1500 Hz, respectively. The EIS measurements were performed with a bias potential of −1.2 V in the dark. Photocurrent measurements were performed on a CHI 760E electrochemical workstation. Typically, 2 mg of photocatalyst was dispersed into 2 mL of ethanol and 10 $\mu$L of Nafion mixed solution. The indium−tin oxide (ITO) glass coated with 1 cm² mixed solution was used as a working electrode. The measurements were carried out using a three-electrode system with a Pt plate as a counter electrode and Ag/AgCl as reference electrode. A 0.1 M $Na_2SO_4$ solution was used as the electrolyte. A 300 W xenon lamp with a UV cutoff filter (>380 nm) was used as the light source. The photocurrent signals of the samples were recorded under a bias potential of +0.5 V. The sample interval was 0.1 s, and the running time was 200 s.

**X-ray Absorption Fine Structure Spectra Measurements.** The X-ray absorption fine structure spectra (XAFS) were collected at the 1W1B station in Beijing Synchrotron Radiation Facility (BSRF). The storage rings of BSRF were operated at 2.5 GeV with an average current of 250 mA. Using a Si(111) double-crystal monochromator, the data collection was carried out in transmission mode using an ionization chamber. All spectra were collected under ambient conditions.

The acquired EXAFS data were processed according to the standard procedures using the ATHENA module implemented in the IFEFFIT software packages.[58] The $k^3$-weighted EXAFS spectra were obtained by subtracting the postedge background from the overall absorption and then normalizing with respect to the edge-jump step.[59] Subsequently, the $k^3$-weighted $\chi(k)$ data of Co K-edge were Fourier transformed to real (R) space using a Hanning windows (dk = 1.0 Å⁻¹) to separate the EXAFS contributions from different coordination shells. To obtain the quantitative structural parameters around central atoms, least-squares curve parameter fitting was performed using the ARTEMIS module of IFEFFIT software packages.[60] The parameters, i.e., coordination number (CN), bond length (R), Debye−Waller factor ($\sigma$2), and $E_0$ shift ($\Delta E_0$) around Co, were allowed to vary during the fit process.

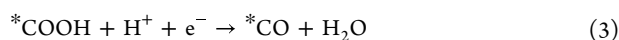**In Situ Soft X-ray Absorption Spectroscopy Measurements.** The *in situ* soft X-ray absorption spectroscopy (sXAS) data were collected at the photoemission end-station of beamline BL10B at the National Synchrotron Radiation Laboratory (NSRL) in Hefei, China. The beamline is connected to a bending magnet and can deliver photon energies in the range of 100 to 1000 eV. It has a resolving power (E/$\Delta E$) exceeding 1000 and a photon flux of $10^9$ photons per second. During the light exposure experiments, the MOF was directly irradiated through the window of the analysis chamber.

**Photocatalytic $CO_2$ Reduction.** The photocatalytic $CO_2$ reduction experiments were performed in a 160 mL optical reaction vessel (Beijing Perfectlight Technology Co., Ltd., China) with stirring at ambient temperature. First, 5 mg of photocatalyst and 25 mg of BIH were dispersed into 25 mL of acetonitrile. After homogeneous mixing, the suspension was stirred and purged with $CO_2$ for ∼20 min. The light source was a 300 W Xe lamp equipped with a UV cutoff filter (>380 nm), unless otherwise specifically stated. For each evaluation of gas generation, 100 $\mu$L of the headspace was injected into the gas chromatography (Agilent 8860, argon as a carrier gas) using a thermal conductivity detector (TCD) and a flame ionization detector (FID). $H_2$, CO, and $CH_4$ were quantified by a calibration plot. The possible liquid products were detected by ion chromatography and $^1$H NMR.

**DFT Calculations.** The density functional theory (DFT) implementation in the CP2K 6.1.0 program[61] was used to optimize different spin hybrid structures. The Quickstep method[62] was based on a hybrid Gaussian plane wave (GPW) scheme[63] with a plane wave cutoff of 500 Ry. The Goedecker−Teter−Hutter (GTH)[64] pseudopotentials were applied to describe the interactions between the core electrons in the calculations. The Perdew−Burke−Ernzerhof (PBE)[65] was used to describe the exchange-correlation effects. To illustrate van der Waals interactions, the Grimme-D3 dispersion correction was applied in all calculations. The localized double $\xi$-valence-polarized basis set (DZVP)[66] was chosen to expand the wave functions.

In static calculations, the hybrid function of Heyd, Scuseria, and Ernzerhof (HSE06)[67] was used to get the energy of structures in the Vienna ab initio simulation package (VASP).[68] The convergence criterion for the electronic self-consistent cycle was fixed at $10^{-5}$ eV. Grimme's DFT-D3 method was applied to the long-range van der Waals (vdW) interaction corrections. The cutoff energy for the plane-wave basis set was set to 400 eV. The Brillouin zone was sampled with $1 \times 1 \times 1$ Monkhorst−Pack k-mesh. To get more accurate results, an implicit solvent acetonitrile was added in all calculations based on the experimental conditions by Hennig and co-workers under the name VASPsol.[69]

**Calculation for the Free Energies.** Based on the general single site of the $CO_2$ reduction ($CO_2$RR) mechanism, the pathway for $CO_2$ reduction of CO in the whole reaction can be written as

$$* + CO_2 \rightarrow {}^*CO_2 \tag{1}$$

$$^*CO_2 + H^+ + e^- \rightarrow {}^*COOH \tag{2}$$

$$^*COOH + H^+ + e^- \rightarrow {}^*CO + H_2O \tag{3}$$

$$^*CO \rightarrow * + CO \tag{4}$$

Here, an asterisk (*) represents the active sites in the MOF catalysts. To calculate the free energy changes, a standard change of Gibbs free energy at zero potential was calculated according to the following standard formual:[70]

$$\Delta G = \Delta E + \Delta ZPE - T\Delta S$$

where $\Delta E$ refers to the change of reaction energy based on DFT simulations, $\Delta ZPE$ is the zero-point energy change calculated by the vibrational frequency using the finite difference method, and $\Delta S$ represents the entropy change for each elementary step. The temperature in our work is set to 298.15 K.

## ■ ASSOCIATED CONTENT

### ⓢ Supporting Information

The Supporting Information is available free of charge at https://pubs.acs.org/doi/10.1021/jacs.3c11446.

> Powder XRD patterns, Co K-edge FT-EXAFS spectra, SEM images, $N_2$ sorption and desorption isotherms, BET surface area plots, $CO_2$ sorption curves, UV–vis diffuse reflectance spectra, Tauc plots, Mott–Schottky plots, and energy diagrams, XPS results, temperature-dependent magnetization curves, plot of modified inverse susceptibility vs temperature, time-dependent plots recording photocatalytic $CO_2$ reduction to CO production, ion chromatography plots, $^1H$ NMR data, powder XRD patterns, EPR spectra, DOS and enlarged DOS diagrams, LSV profiles, EIS plots, photocurrent responses, PL emission spectra, curve fitting for the time-resolved PL spectrum, EXAFS fitting parameters at the Co K-edge, calculated energies of the Co-based MOF photocatalysts with different spin states, photocatalytic $CO_2$ reduction performance, comparison of CO activity and selectivity of **Co-OAc** with previously reported heterogeneous photocatalysts (PDF)

## ■ AUTHOR INFORMATION

### Corresponding Authors

**Jun Jiang** − *Key Laboratory of Precision and Intelligent Chemistry, University of Science and Technology of China, Hefei, Anhui 230026, P. R. China;* ⓞ orcid.org/0000-0002-6116-5605; Email: jiangj1@ustc.edu.cn

**Hai-Long Jiang** − *Hefei National Research Center for Physical Sciences at the Microscale, Department of Chemistry, University of Science and Technology of China, Hefei, Anhui 230026, P. R. China;* ⓞ orcid.org/0000-0002-2975-7977; Email: jianglab@ustc.edu.cn

### Authors

**Kang Sun** − *Hefei National Research Center for Physical Sciences at the Microscale, Department of Chemistry, University of Science and Technology of China, Hefei, Anhui 230026, P. R. China*

**Yan Huang** − *Key Laboratory of Precision and Intelligent Chemistry, University of Science and Technology of China, Hefei, Anhui 230026, P. R. China*

**Qingyu Wang** − *Hefei National Research Center for Physical Sciences at the Microscale, Department of Chemistry, University of Science and Technology of China, Hefei, Anhui 230026, P. R. China; National Synchrotron Radiation Laboratory (NSRL), University of Science and Technology of China, Hefei, Anhui 230029, P. R. China*

**Wendi Zhao** − *Hefei National Research Center for Physical Sciences at the Microscale, Department of Chemistry, University of Science and Technology of China, Hefei, Anhui 230026, P. R. China*

**Xusheng Zheng** − *National Synchrotron Radiation Laboratory (NSRL), University of Science and Technology of China, Hefei, Anhui 230029, P. R. China;* ⓞ orcid.org/0000-0003-2559-6106

Complete contact information is available at:
https://pubs.acs.org/10.1021/jacs.3c11446

### Author Contributions

[#]K.S and Y.H. contributed equally to this paper.

### Notes

The authors declare no competing financial interest.

## ■ REFERENCES

(1) Chu, S.; Cui, Y.; Liu, N. The path towards sustainable energy. *Nat. Mater.* **2017**, *16*, 16−22.

(2) Lin, H.; Luo, S.; Zhang, H.; Ye, J. Toward solar-driven carbon recycling. *Joule* **2022**, *6*, 294−314.

(3) Gong, E.; Ali, S.; Hiragond, C. B.; Kim, H. S.; Powar, N. S.; Kim, D.; Kim, H.; In, S.-I. Solar fuels: research and development strategies to accelerate photocatalytic $CO_2$ conversion into hydrocarbon fuels. *Energy Environ. Sci.* **2022**, *15*, 880−937.

(4) Velty, A.; Corma, A. Advanced zeolite and ordered mesoporous silica-based catalysts for the conversion of $CO_2$ to chemicals and fuels. *Chem. Soc. Rev.* **2023**, *52*, 1773−1946.

(5) White, J. L.; Baruch, M. F.; Pander, J. E., III; Hu, Y.; Fortmeyer, I. C.; Park, J. E.; Zhang, T.; Liao, K.; Gu, J.; Yan, Y.; Shaw, T. W.; Abelev, E.; Bocarsly, A. B. Light-driven heterogeneous reduction of carbon dioxide: photocatalysts and photoelectrodes. *Chem. Rev.* **2015**, *115*, 12888−12935.

(6) Dong, X.-Y.; Si, Y.-N.; Wang, Q.-Y.; Wang, S.; Zang, S.-Q. Integrating single atoms with different microenvironments into one porous organic polymer for efficient photocatalytic $CO_2$ reduction. *Adv. Mater.* **2021**, *33*, 2101568.

(7) Yang, G.; Li, S.; Li, N.; Zhang, P.; Su, C.; Gong, L.; Chen, B.; Qu, C.; Qi, D.; Wang, T.; Jiang, J. Enhanced photocatalytic CO2 reduction through hydrophobic microenvironment and binuclear Cobalt synergistic effect in metallogels. *Angew. Chem., Int. Ed.* **2022**, *61*, No. e202205585.

(8) Ou, H.; Li, G.; Ren, W.; Pan, B.; Luo, G.; Hu, Z.; Wang, D.; Li, Y. Atomically dispersed Au-assisted C−C coupling on red phosphorus for $CO_2$ photoreduction to $C_2H_6$. *J. Am. Chem. Soc.* **2022**, *144*, 22075−22082.

(9) Rodríguez-Jiménez, S.; Song, H.; Lam, E.; Wright, D.; Pannwitz, A.; Bonke, S. A.; Baumberg, J. J.; Bonnet, S.; Hammarström, L.; Reisner, E. Self-assembled liposomes enhance electron transfer for efficient photocatalytic $CO_2$ reduction. *J. Am. Chem. Soc.* **2022**, *144*, 9399−9412.

(10) Zhang, Y.; Zhi, X.; Harmer, J. R.; Xu, H.; Davey, K.; Ran, J.; Qiao, S.-Z. Facet-specific active surface regulation of $Bi_xMO_y$ (M = Mo, V, W) nanosheets for boosted photocatalytic $CO_2$ reduction. *Angew. Chem., Int. Ed.* **2022**, *61*, e202212355.

(11) Snyder, B. E. R.; Vanelderen, P.; Bols, M. L.; Hallaert, S. D.; Böttger, L. H.; Ungur, L.; Pierloot, K.; Schoonheydt, R. A.; Sels, B. F.;

Solomon, E. I. The active site of low-temperature methane hydroxylation in iron-containing zeolites. *Nature* **2016**, *536*, 317−321.

(12) Li, Y.; Wang, Z.; Wang, Y.; Kovács, A.; Foo, C.; Dunin-Borkowski, R. E.; Lu, Y.; Taylor, R. A.; Wu, C.; Tsang, S. C. E. Local magnetic spin mismatch promoting photocatalytic overall water splitting with exceptional solar-to-hydrogen efficiency. *Energy Environ. Sci.* **2022**, *15*, 265−277.

(13) Yan, J.; Kong, L.; Ji, Y.; White, J.; Li, Y.; Zhang, J.; An, P.; Liu, S.; Lee, S.-T.; Ma, T. Single atom tungsten doped ultrathin α-Ni(OH)$_2$ for enhanced electrocatalytic water oxidation. *Nat. Commun.* **2019**, *10*, 2149.

(14) Zhao, Z.; Wang, D.; Gao, R.; Wen, G.; Feng, M.; Song, G.; Zhu, J.; Luo, D.; Tan, H.; Ge, X.; Zhang, W.; Zhang, Y.; Zheng, L.; Li, H.; Chen, Z. Magnetic-field-stimulated efficient photocatalytic N$_2$ fixation over defective BaTiO$_3$ perovskites. *Angew. Chem., Int. Ed.* **2021**, *60*, 11910−11918.

(15) He, J.; Hu, L.; Shao, C.; Jiang, S.; Sun, C.; Song, S. Photocatalytic H$_2$O overall splitting into H$_2$ bubbles by single atomic sulfur vacancy CdS with spin polarization electric field. *ACS Nano* **2021**, *15*, 18006−18013.

(16) Pan, L.; Ai, M.; Huang, C.; Yin, L.; Liu, X.; Zhang, R.; Wang, S.; Jiang, Z.; Zhang, X.; Zou, J.-J.; Mi, W. Manipulating spin polarization of titanium dioxide for efficient photocatalysis. *Nat. Commun.* **2020**, *11*, 418.

(17) Zhong, W.; Qiu, Y.; Shen, H.; Wang, X.; Yuan, J.; Jia, C.; Bi, S.; Jiang, J. Electronic spin moment As a catalytic descriptor for Fe single-atom catalysts supported on C$_2$N. *J. Am. Chem. Soc.* **2021**, *143*, 4405−4413.

(18) Gong, Y.-N.; Zhong, W.; Li, Y.; Qiu, Y.; Zheng, L.; Jiang, J.; Jiang, H.-L. Regulating photocatalysis by spin-state manipulation of cobalt in covalent organic frameworks. *J. Am. Chem. Soc.* **2020**, *142*, 16723−16731.

(19) Lin, C.-C.; Liu, T.-R.; Lin, S.-R.; Boopathi, K. M.; Chiang, C.-H.; Tzeng, W.-Y.; Chien, W.-H. C.; Hsu, H.-S.; Luo, C.-W.; Tsai, H.-Y.; Chen, H.-A.; Kuo, P.-C.; Shiue, J.; Chiou, J.-W.; Pong, W.-F.; Chen, C.-C.; Chen, C.-W. Spin-polarized photocatalytic CO$_2$ reduction of Mn-doped perovskite nanoplates. *J. Am. Chem. Soc.* **2022**, *144*, 15718−15726.

(20) Wu, D.; Yin, H.; Wang, Z.; Zhou, M.; Yu, C.; Wu, J.; Miao, H.; Yamamoto, T.; Zhaxi, W.; Huang, Z.; Liu, L.; Huang, W.; Zhong, W.; Einaga, Y.; Jiang, J.; Zhang, Z. Spin manipulation in a metal−organic layer through mechanical exfoliation for highly selective CO$_2$ photoreduction. *Angew. Chem., Int. Ed.* **2023**, *62*, e202301925.

(21) Furukawa, H.; Cordova, K. E.; O'Keeffe, M.; Yaghi, O. M. The chemistry and applications of metal-organic frameworks. *Science* **2013**, *341*, 1230444.

(22) Zhou, H.-C. J.; Kitagawa, S. Metal−organic frameworks (MOFs). *Chem. Soc. Rev.* **2014**, *43*, 5415−5418.

(23) Yao, Y.; Zhao, X.; Chang, G.; Yang, X.; Chen, B. Hierarchically porous metal−organic frameworks: synthetic strategies and applications. *Small Struct.* **2023**, *4*, 2200187.

(24) Zhao, X.; Wang, Y.; Li, D.-S.; Bu, X.; Feng, P. Metal−organic frameworks for separation. *Adv. Mater.* **2018**, *30*, 1705189.

(25) Huang, Y.-B.; Liang, J.; Wang, X.-S.; Cao, R. Multifunctional metal−organic framework catalysts: synergistic catalysis and tandem reactions. *Chem. Soc. Rev.* **2017**, *46*, 126−157.

(26) Zhang, H.; Nai, J.; Yu, L.; Lou, X. W. Metal-organic-framework-based materials as platforms for renewable energy and environmental applications. *Joule* **2017**, *1*, 77−107.

(27) Li, G.; Zhao, S.; Zhang, Y.; Tang, Z. Metal−organic frameworks encapsulating active nanoparticles as emerging composites for catalysis: recent progress and perspectives. *Adv. Mater.* **2018**, *30*, 1800702.

(28) Wei, Y.-S.; Zhang, M.; Zou, R.; Xu, Q. Metal−organic framework-based catalysts with single metal sites. *Chem. Rev.* **2020**, *120*, 12089−12174.

(29) Nyakuchena, J.; Ostresh, S.; Streater, D.; Pattengale, B.; Neu, J.; Fiankor, C.; Hu, W.; Kinigstein, E. D.; Zhang, J.; Zhang, X.; Schmuttenmaer, C. A.; Huang, J. Direct evidence of photoinduced charge transport mechanism in 2D conductive metal organic frameworks. *J. Am. Chem. Soc.* **2020**, *142*, 21050−21058.

(30) Liu, J.; Goetjen, T. A.; Wang, Q.; Knapp, J. G.; Wasson, M. C.; Yang, Y.; Syed, Z. H.; Delferro, M.; Notestein, J. M.; Farha, O. K.; Hupp, J. T. MOF-enabled confinement and related effects for chemical catalyst presentation and utilization. *Chem. Soc. Rev.* **2022**, *51*, 1045−1097.

(31) Jiao, L.; Wang, J.; Jiang, H.-L. Microenvironment modulation in metal−organic framework-based catalysis. *Acc. Mater. Res.* **2021**, *2*, 327−339.

(32) Sun, K.; Qian, Y.; Jiang, H.-L. Metal-organic frameworks for photocatalytic water splitting and CO$_2$ reduction. *Angew. Chem., Int. Ed.* **2023**, *62*, e202217565.

(33) Fu, Y.; Sun, D.; Chen, Y.; Huang, R.; Ding, Z.; Fu, X.; Li, Z. An Amine-functionalized titanium metal−organic framework photocatalyst with visible-light-induced activity for CO$_2$ reduction. *Angew. Chem., Int. Ed.* **2012**, *51*, 3364−3367.

(34) Xu, H.-Q.; Hu, J.; Wang, D.; Li, Z.; Zhang, Q.; Luo, Y.; Yu, S.-H.; Jiang, H.-L. Visible-light photoreduction of CO$_2$ in a metal−organic framework: boosting electron−hole separation via electron trap states. *J. Am. Chem. Soc.* **2015**, *137*, 13440−13443.

(35) Dong, L.-Z.; Zhang, L.; Liu, J.; Huang, Q.; Lu, M.; Ji, W.-X.; Lan, Y.-Q. Stable heterometallic cluster-based organic framework catalysts for artificial photosynthesis. *Angew. Chem., Int. Ed.* **2020**, *59*, 2659−2663.

(36) Yang, W.; Wang, H.-J.; Liu, R.-R.; Wang, J.-W.; Zhang, C.; Li, C.; Zhong, D.-C.; Lu, T.-B. Tailoring crystal facets of metal−organic layers to enhance photocatalytic activity for CO$_2$ reduction. *Angew. Chem., Int. Ed.* **2021**, *60*, 409−414.

(37) Ghosh, A. C.; Legrand, A.; Rajapaksha, R.; Craig, G. A.; Sassoye, C.; Balázs, G.; Farrusseng, D.; Furukawa, S.; Canivet, J.; Wisser, F. M. Rhodium-based metal−organic polyhedra assemblies for selective CO$_2$ photoreduction. *J. Am. Chem. Soc.* **2022**, *144*, 3626−3636.

(38) Karmakar, S.; Barman, S.; Rahimi, F. A.; Biswas, S.; Nath, S.; Maji, T. K. Developing post-modified Ce-MOF as a photocatalyst: a detail mechanistic insight into CO$_2$ reduction toward selective C$_2$ product formation. *Energy Environ. Sci.* **2023**, *16*, 2187−2198.

(39) Guo, F.; Li, R.-L.; Yang, S.; Zhang, X.-Y.; Yu, H.; Urban, J. J.; Sun, W.-Y. Designing heteroatom-codoped iron metal−organic framework for promotional photoreduction of carbon dioxide to ethylene. *Angew. Chem., Int. Ed.* **2023**, *62*, e202216232.

(40) Zhang, T.; Lin, W. Metal−organic frameworks for artificial photosynthesis and photocatalysis. *Chem. Soc. Rev.* **2014**, *43*, 5982−5993.

(41) Xiao, J.-D.; Jiang, H.-L. Metal−organic frameworks for photocatalysis and photothermal catalysis. *Acc. Chem. Res.* **2019**, *52*, 356−366.

(42) Zeng, L.; Guo, X.; He, C.; Duan, C. Metal−organic frameworks: versatile materials for heterogeneous photocatalysis. *ACS Catal.* **2016**, *6*, 7935−7947.

(43) Navalón, S.; Dhakshinamoorthy, A.; Álvaro, M.; Ferrer, B.; García, H. Metal−organic frameworks as photocatalysts for solar-driven overall water splitting. *Chem. Rev.* **2023**, *123*, 445−490.

(44) Ma, X.; Liu, H.; Yang, W.; Mao, G.; Zheng, L.; Jiang, H.-L. Modulating coordination environment of single-atom catalysts and their proximity to photosensitive units for boosting MOF photocatalysis. *J. Am. Chem. Soc.* **2021**, *143*, 12220−12229.

(45) Schmieder, P.; Denysenko, D.; Grzywa, M.; Baumgärtner, B.; Senkovska, I.; Kaskel, S.; Sastre, G.; van Wüllen, L.; Volkmer, D. CFA-1: the first chiral metal−organic framework containing Kuratowski-type secondary building units. *Dalton Trans.* **2013**, *42*, 10786−10797.

(46) Brown, D. G.; Weser, U. XPS spectra of spin-triplet Cobalt(III) complexes. *Z. Naturforsch. B* **1979**, *34*, 1468−1470.

(47) Wu, K.-H.; Liu, Y.; Tan, X.; Liu, Y.; Lin, Y.; Huang, X.; Ding, Y.; Su, B.-J.; Zhang, B.; Chen, J.-M.; Yan, W.; Smith, S. C.; Gentle, I. R.; Zhao, S. Regulating electron transfer over asymmetric low-spin Co(II) for highly selective electrocatalysis. *Chem. Catal.* **2022**, *2*, 372−385.

(48) Mugiraneza, S.; Hallas, A. M. Tutorial: a beginner's guide to interpreting magnetic susceptibility data with the Curie-Weiss law. *Commun. Phys.* **2022**, *5*, 95.

(49) Shen, G.; Zhang, R.; Pan, L.; Hou, F.; Zhao, Y.; Shen, Z.; Mi, W.; Shi, C.; Wang, Q.; Zhang, X.; Zou, J.-J. Regulating the spin state of feiii by atomically anchoring on ultrathin titanium dioxide for efficient oxygen evolution electrocatalysis. *Angew. Chem., Int. Ed.* **2020**, *59*, 2313–2317.

(50) Wang, Q.; Zhang, Y.; Lin, M.; Wang, H.; Bai, Y.; Liu, C.; Lu, J.; Luo, Q.; Wang, G.; Jiang, H.; Yao, T.; Zheng, X. Photoinduced Metastable Asymmetric Cu Single Atoms for Photoreduction of $CO_2$ to Ethylene. *Adv. Energy Mater.* **2023**, *13*, 2302692.

(51) Zamani, S.; Carter, E.; Murphy, D. M.; Van Doorslaer, S. Probing differences in binding of methylbenzylamine enantiomers to chiral cobalt(ii) salen complexes. *Dalton Trans.* **2012**, *41*, 6861–6870.

(52) Liu, H.; Zhang, F.; Wang, H.; Xue, J.; Guo, Y.; Qian, Q.; Zhang, G. Oxygen vacancy engineered unsaturated coordination in cobalt carbonate hydroxide nanowires enables highly selective photocatalytic $CO_2$ reduction. *Energy Environ. Sci.* **2021**, *14*, 5339–5346.

(53) Ruan, Q.; Miao, T.; Wang, H.; Tang, J. Insight on shallow trap states-introduced photocathodic performance in n-type polymer photocatalysts. *J. Am. Chem. Soc.* **2020**, *142*, 2795–2802.

(54) Li, J.; Huang, H.; Xue, W.; Sun, K.; Song, X.; Wu, C.; Nie, L.; Li, Y.; Liu, C.; Pan, Y.; Jiang, H.-L.; Mei, D.; Zhong, C. Self-adaptive dual-metal-site pairs in metal-organic frameworks for selective $CO_2$ photoreduction to $CH_4$. *Nat. Catal.* **2021**, *4*, 719–729.

(55) Neaţu, Ş.; Maciá-Agulló, J. A.; Concepción, P.; Garcia, H. Gold–copper nanoalloys supported on $TIO_2$ as photocatalysts for $CO_2$ reduction by water. *J. Am. Chem. Soc.* **2014**, *136*, 15969–15976.

(56) Bien, C. E.; Chen, K. K.; Chien, S.-C.; Reiner, B. R.; Lin, L.-C.; Wade, C. R.; Ho, W. S. W. Bioinspired metal-organic framework for trace $CO_2$ capture. *J. Am. Chem. Soc.* **2018**, *140*, 12662–12666.

(57) Hu, Y.; Zhan, F.; Wang, Q.; Sun, Y.; Yu, C.; Zhao, X.; Wang, H.; Long, R.; Zhang, G.; Gao, C.; Zhang, W.; Jiang, J.; Tao, Y.; Xiong, Y. Tracking mechanistic pathway of photocatalytic $CO_2$ reaction at ni sites using operando, time-resolved spectroscopy. *J. Am. Chem. Soc.* **2020**, *142*, 5618–5626.

(58) Ravel, B.; Newville, M. ATHENA, ARTEMIS, HEPHAESTUS: data analysis for X-ray absorption spectroscopy using IFEFFIT. *J. Synchrotron Radiat.* **2005**, *12*, 537–541.

(59) Koningsberger, D. C.; Prins, R. *X-ray absorption: principles, applications, techniques of EXAFS, SEXAFS, and XANES, Chemical Analysis 92*; Wiley: 1988.

(60) Rehr, J. J.; Albers, R. C. Theoretical approaches to x-ray absorption fine structure. *Rev. Mod. Phys.* **2000**, *72*, 621–654.

(61) Kühne, T. D.; Iannuzzi, M.; Del Ben, M.; Rybkin, V. V.; Seewald, P.; Stein, F.; Laino, T.; Khaliullin, R. Z.; Schütt, O.; Schiffmann, F.; Golze, D.; Wilhelm, J.; Chulkov, S.; Bani-Hashemian, M. H.; Weber, V.; Borŝtnik, U.; Taillefumier, M.; Jakobovits, A. S.; Lazzaro, A.; Pabst, H.; Müller, T.; Schade, R.; Guidon, M.; Andermatt, S.; Holmberg, N.; Schenter, G. K.; Hehn, A.; Bussy, A.; Belleflamme, F.; Tabacchi, G.; Glöß, A.; Lass, M.; Bethune, I.; Mundy, C. J.; Plessl, C.; Watkins, M.; VandeVondele, J.; Krack, M.; Hutter, J. CP2K: An electronic structure and molecular dynamics software package - Quickstep: Efficient and accurate electronic structure calculations. *J. Chem. Phys.* **2020**, *152*, 194103.

(62) VandeVondele, J.; Krack, M.; Mohamed, F.; Parrinello, M.; Chassaing, T.; Hutter, J. Quickstep: Fast and accurate density functional calculations using a mixed Gaussian and plane waves approach. *Comput. Phys. Commun.* **2005**, *167*, 103–128.

(63) Lippert, B. G.; Parrinello, J. H.; Michele. A hybrid Gaussian and plane wave density functional scheme. *Mol. Phys.* **1997**, *92*, 477–488.

(64) VandeVondele, J.; Hutter, J. Gaussian basis sets for accurate calculations on molecular systems in gas and condensed phases. *J. Chem. Phys.* **2007**, *127*, 114105.

(65) Perdew, J. P.; Burke, K.; Ernzerhof, M. Generalized gradient approximation made simple. *Phys. Rev. Lett.* **1997**, *78*, 1396–1396.

(66) Hartwigsen, C.; Goedecker, S.; Hutter, J. Relativistic separable dual-space Gaussian pseudopotentials from H to Rn. *Phys. Rev. B* **1998**, *58*, 3641–3662.

(67) Krukau, A. V.; Vydrov, O. A.; Izmaylov, A. F.; Scuseria, G. E. Influence of the exchange screening parameter on the performance of screened hybrid functionals. *J. Chem. Phys.* **2006**, *125*, 224106.

(68) Kresse, G.; Furthmüller, J. Efficient iterative schemes for ab initio total-energy calculations using a plane-wave basis set. *Comput. Mater. Sci.* **1996**, *6*, 15–50.

(69) Mathew, K.; Sundararaman, R.; Letchworth-Weaver, K.; Arias, T. A.; Hennig, R. G. Implicit solvation model for density-functional study of nanocrystal surfaces and reaction pathways. *J. Chem. Phys.* **2014**, *140*, No. 084106.

(70) Nørskov, J. K.; Rossmeisl, J.; Logadottir, A.; Lindqvist, L.; Kitchin, J. R.; Bligaard, T.; Jónsson, H. Origin of the overpotential for oxygen reduction at a fuel-cell cathode. *J. Phys. Chem. B* **2004**, *108*, 17886–17892.